




Received April 23, 2023; accepted January 28, 2024; Date of publication March 26, 2024.   
The review of this paper was arranged by Associate Editor Heverton A. Pereira  and Editor-in-Chief Telles Brunelli Lazzarin .

Digital Object Identifier <http://doi.org/10.18618/REP.2024.1.0011>

# Experimental Assessment of Predictive Current Control Applied to Induction Machine Drive Systems Operating Under Single-Phase Open-Circuit Fault

Liane M. de Oliveira <sup>1</sup>, Victor F. M. B. Melo <sup>1</sup>, Gilielson F. da Paz <sup>2,3</sup>, Filipe V. Rocha <sup>3</sup>, Edgard L. L. Fabrício <sup>4</sup>

<sup>1</sup>Federal University of Paraíba, Dept. of Renewable Energies Engineering, João Pessoa, PB, Brazil

<sup>2</sup>Federal University of Paraíba, Dept. of Electrical Engineering, João Pessoa, PB, Brazil

<sup>3</sup>Federal University of Campina Grande, Dept. of Electrical Engineering, Campina Grande, PB, Brazil

<sup>4</sup>Federal Institute of Paraíba, Dept. of Electrical Engineering, João Pessoa, PB, Brazil

e-mail: liane.oliveira@cear.ufpb.br, victor@cear.ufpb.br, gilielson@cear.ufpb.br,  
filipe.rocha@ee.ufcg.edu.br, edgard.fabricio@ifpb.edu.br

**ABSTRACT** Predictive Current Control (PCC) has been widely applied in several applications. However, the literature has not discussed its use as a fault tolerance control algorithm in induction drive systems. In this way, this paper discusses the PCC method in two fault-tolerant squirrel-cage induction machine drive systems operating under single-phase open-circuit faults. PCC's postfault performance is compared to Field Oriented Control (FOC) for different steady- and transient-state scenarios, analyzing harmonic distortion, torque ripple, and the transition from healthy to postfault operation. Also, experiments tested the robustness of postfault PCC to low-speed operation, parametric variation, and a step change in reference rotor speed, showing that PCC also presents fault-tolerant operation under these conditions.

**KEYWORDS** Fault-Tolerance, FCS-MPC, Induction Machine Drive Systems, Predictive Current Control.

## I. INTRODUCTION

Nowadays, several control methods may be employed in induction machine (IM) drives, being the Field Oriented Control (FOC), proposed in [1], and the Direct Torque Control (DTC), first discussed in [2], [3], the most common methods [4]. However, more recently, the Finite Control Set – Model Predictive Control (FCS-MPC) has gained a lot of attention for power electronics applications. It is due to its advantages when compared to other methods, such as fast transient response, simplicity in taking into account non-linear constraints, and multiple variable control. Also, there is no need for a proportional-integral (PI) current controllers design [5], [6].

In this way, for electric machines control, two types of FCS-MPC are usually employed [7]. The first type is the Predictive Torque Control (PTC), which directly adjusts the stator flux magnitude and the machine electromagnetic torque. In this case, the cost function to be minimized is

based on the stator flux and torque errors. The second type of FCS-MPC is the Predictive Current Control (PCC), in which the stator  $\alpha\beta$  current components are adjusted by means of the minimization of a cost function based on the current error. In [7], the authors carried out a performance comparison between the two control strategies for a three-phase induction motor drive, concluding that PTC provides a lower torque ripple and a lower flux ripple than PCC. In contrast, PCC provides a lower current ripple than PTC. Considering the dynamic performance, both methods performed very similarly. Recently, several papers have discussed the use of model predictive control in machine drive systems, such as [8]–[11] for induction machine control and [12], [13] for Permanent-Magnet Synchronous Machine (PMSM) control.

On the other hand, there are several kinds of faults in drive systems. However, one of the most studied is the single-phase open-circuit fault, in which one of the machine

phases is disconnected from the converter. When a single-phase open-circuit fault occurs, the drive system must be physically reconfigured (usually by triacs) to keep a circular flux trajectory after the fault (necessary condition for the machine operate properly). Also, its control algorithm and Pulse Width Modulation (PWM) strategy must be adapted to the faulty condition. In 2004, Welchko *et al.* [14] provided a survey on fault-tolerant inverter topologies and strategies for three-phase ac drives. Still, all of the reported papers make use of FOC-based compensation strategies.

Still today, fault tolerance for ac drives is a hot topic. Concerning the single-phase open-circuit fault, [15] discussed the use of FCS-MPC for a fault-tolerant PMSM drive system. The authors used PTC as fault compensation strategy, showing that this control provides fault-tolerant operation. Also, for PMSM drives, in [16], a resonant-based controller was studied to suppress the postfault second harmonic torque and speed ripples that take place, which is achieved by adequately modelling the system and designing the controller. On the other hand, for induction machine drive systems, in [17], the authors discussed the use of DTC for three fault-tolerant induction squirrel-cage motor drive systems for the case of single-phase open-circuit fault. DTC method provides a circular flux trajectory, and the systems operate correctly. For the same type of fault, [18] discussed voltage, current, and speed limitations for four fault-tolerant topologies for induction machine control.

In this context, the discussion of postfault FCS-MPC for three-phase squirrel-cage induction machine drives, along with fault-tolerant converters, is lacking in the literature. Thus, the present paper discusses two fault-tolerant induction machine drive systems operating with single-phase open-circuit fault employing the Predictive Current Control strategy. This paper is an extended version of the conference paper [19]. In this new version, the authors provide a more profound discussion of the PCC method and its steady- and transient-state performances for two of the three configurations discussed in [19], as well as new experimental results. The main contributions of this paper are showing that the PCC method (*i*) provides fault-tolerant operation for both high and low rotor speeds, (*ii*) is robust to variation in stator resistance and mutual inductance in postfault operation, (*iii*) presents a good dynamic response to step change in rotor speed. Also, the paper compares FOC and PCC in terms of postfault current total harmonic distortion (THD) and torque ripple, as well as dynamic response considering the migration from healthy to postfault operation.

## II. FAULT-TOLERANT INVERTERS

Both studied configurations are illustrated in Figure 1. During healthy operation, all triacs are blocked. In the occurrence of a single-phase open-circuit fault, the systems must be physically reconfigured, as well as the control algorithm. Suppose the fault occurs in one of the machine phases for configuration 1, the triac TR is activated, and the machine

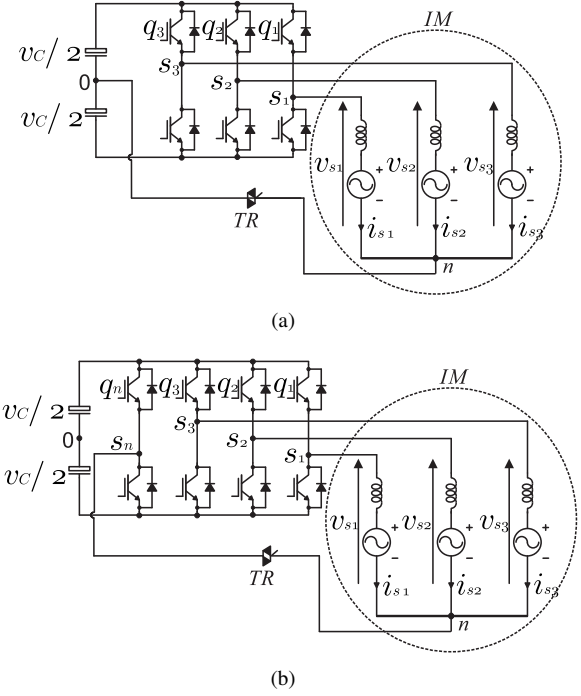


FIGURE 1. Fault-tolerant drive systems. (a) Configuration 1. (b) Configuration 2.

neutral is connected to the dc-link mid-point. On the other hand, for configuration 2, the reconfiguration consists in connecting the machine neutral to an extra leg through a triac TR.

## III. INDUCTION MACHINE MODEL

In order to obtain the three-phase squirrel-cage induction machine model, the machine's primary variables are transformed into a two-dimensional domain, usually named  $\alpha\beta$ , and a single-dimensional domain, usually named  $o$ , which represents the zero-sequence component. The transformation from one domain to the other is given as follows:

$$f_s \alpha\beta o = P_s^T f_s 123 \quad (1)$$

where  $f_s 123 = [f_{s1} \ f_{s2} \ f_{s3}]^T$  is the machine primary variables matrix and  $f_s \alpha\beta o = [f_{s\alpha} \ f_{s\beta} \ f_{so}]^T$  is the machine  $\alpha\beta$  variables matrix. These variables may be stator voltages ( $f = v$ ), stator currents ( $f = i$ ) or stator fluxes ( $f = \phi$ ). Matrix  $P_s$  is obtained considering the stationary common reference frame and is given by

$$P_s = \sqrt{\frac{2}{3}} \begin{bmatrix} 1 & 0 & \frac{1}{\sqrt{2}} \\ -\frac{1}{2} & \frac{\sqrt{3}}{2} & \frac{1}{\sqrt{2}} \\ -\frac{1}{2} & -\frac{\sqrt{3}}{2} & \frac{1}{\sqrt{2}} \end{bmatrix}. \quad (2)$$

Under motoring convention, the machine equations in  $\alpha\beta$  model are

$$v_{s\alpha} = r_s i_{s\alpha} + \frac{d\phi_{s\alpha}}{dt} \quad (3)$$

$$v_{s\beta} = r_s i_{s\beta} + \frac{d\phi_{s\beta}}{dt} \quad (4)$$

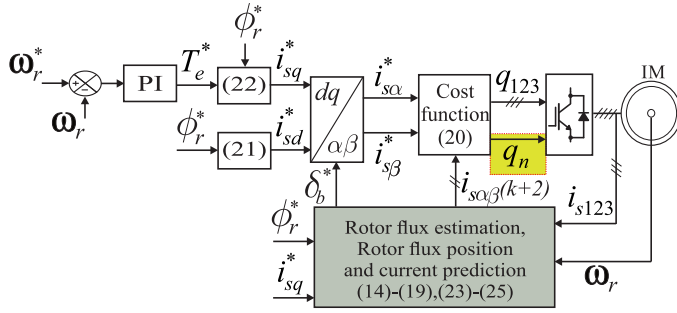


FIGURE 2. Control system diagram.

$$v_{s0} = r_s i_{s0} + L_{ls} \frac{di_{s0}}{dt} \quad (5)$$

$$0 = r_r i_{r\alpha} + \frac{d\phi_{r\alpha}}{dt} + \phi_{r\beta} \omega_r \quad (6)$$

$$0 = r_r i_{r\beta} + \frac{d\phi_{r\beta}}{dt} - \phi_{r\alpha} \omega_r \quad (7)$$

$$\phi_{s\alpha} = L_s i_{s\alpha} + L_m i_{r\alpha} \quad (8)$$

$$\phi_{s\beta} = L_s i_{s\beta} + L_m i_{r\beta} \quad (9)$$

$$\phi_{s0} = L_{ls} i_{s0} \quad (10)$$

$$\phi_{r\alpha} = L_r i_{r\alpha} + L_m i_{s\alpha} \quad (11)$$

$$\phi_{r\beta} = L_r i_{r\beta} + L_m i_{s\beta} \quad (12)$$

$$T_e = p(\phi_{s\alpha} i_{s\beta} - \phi_{s\beta} i_{s\alpha}) \quad (13)$$

where  $r_s$  and  $r_r$  are the stator and rotor windings resistance, respectively,  $L_s$  and  $L_r$  are the equivalent self-inductance of the stator and rotor windings, respectively,  $L_m$  is the stator-rotor equivalent mutual inductance and  $L_{ls}$  is the stator leakage inductance.  $i_{r\alpha}$  and  $i_{r\beta}$  are the rotor  $\alpha\beta$  currents in the stationary reference frame,  $\omega_r$  is the rotor electrical speed in rad/s,  $T_e$  is the electromagnetic torque, and  $p$  is the number of pole pairs.

#### IV. PREDICTIVE CURRENT CONTROL

The PCC algorithm for squirrel-cage induction machine drives is based on the mathematical model shown in (3)–(12). The control system is illustrated in Figure 2.

Since the method controls the  $\alpha\beta$  currents, they must be predicted, as shown in [7]. Also, considering the delay compensation, which is necessary to achieve low current ripple, as discussed in [6], these current components must be predicted using a two-step horizon (i.e.,  $k+2$ ). In this way, from the model equations, the predicted  $\alpha\beta$  currents are

$$i_{s\alpha}(k+2) = \{v_{s\alpha}(k+2) + \sigma L_s i_{s\alpha}(k+1)/T_s + L_m/L_r[\phi_{r\alpha}(k+1)/\tau_r + \omega_r \phi_{r\beta}(k+1)]\}/(r_\sigma + \sigma L_s/T_s) \quad (14)$$

$$i_{s\beta}(k+2) = \{v_{s\beta}(k+2) + \sigma L_s i_{s\beta}(k+1)/T_s + L_m/L_r[\phi_{r\beta}(k+1)/\tau_r - \omega_r \phi_{r\alpha}(k+1)]\}/(r_\sigma + \sigma L_s/T_s) \quad (15)$$

where  $\tau_r$  is the rotor time constant ( $\tau_r = L_r/r_r$ ),  $\sigma$  is the leakage factor [ $\sigma = 1 - L_m^2/(L_s L_r)$ ],  $\phi_{r\alpha}(k+1)$  and  $\phi_{r\beta}(k+1)$

are the rotor flux  $\alpha\beta$  components in step  $k+1$ , and  $T_s$  is the sampling period. Also,  $r_\sigma = r_s + r_r L_m^2/L_r^2$ .

$$\phi_{r\alpha}(k+1) = L_m T_s i_{s\alpha}(k)/\tau_r + (1 - T_s/\tau_r)\phi_{r\alpha}(k) - T_s \omega_r \phi_{r\beta}(k) \quad (16)$$

$$\phi_{r\beta}(k+1) = L_m T_s i_{s\beta}(k)/\tau_r + (1 - T_s/\tau_r)\phi_{r\beta}(k) + T_s \omega_r \phi_{r\alpha}(k). \quad (17)$$

In turn, the rotor fluxes  $\phi_{r\alpha}(k)$  and  $\phi_{r\beta}(k)$  are

$$\phi_{r\alpha}(k) = L_r \phi_{s\alpha}(k)/L_m - \sigma L_s L_r i_{s\alpha}(k)/L_m \quad (18)$$

$$\phi_{r\beta}(k) = L_r \phi_{s\beta}(k)/L_m - \sigma L_s L_r i_{s\beta}(k)/L_m \quad (19)$$

where the stator flux  $\alpha\beta$  components  $\phi_{s\alpha}(k)$  and  $\phi_{s\beta}(k)$  are estimated using the observer discussed in [20].

Thus, the cost function for the PCC method is

$$g = (i_{s\alpha}^* - i_{s\alpha}(k+2))^2 + (i_{s\beta}^* - i_{s\beta}(k+2))^2 \quad (20)$$

where  $i_{s\alpha}^*$  and  $i_{s\beta}^*$  are the  $\alpha\beta$  reference currents. The cost function (20) is valid for both healthy and post-fault operations.

The reference currents  $i_{s\alpha}^*$  and  $i_{s\beta}^*$  are obtained by first defining the values of  $dq$  stator current components in the rotor flux reference frame. They are given by

$$i_{sd}^* = \frac{\phi_r^*}{L_m} \quad (21)$$

$$i_{sq}^* = \frac{L_r T_e^*}{L_m \phi_r^*} \quad (22)$$

where  $\phi_r^*$  is the reference amplitude of the rotor flux and  $T_e^*$  is the reference electromagnetic torque, which is provided by a proportional-integral (PI) speed controller.

The reference slip value is given by

$$\omega_{br}^* = \frac{L_m i_{sq}^*}{\phi_r^* \tau_r}. \quad (23)$$

Then, the reference rotor flux speed is given by

$$\omega_b^* = \omega_r + \omega_{br}^* \quad (24)$$

and the rotor flux position is

$$\delta_b^* = \int \omega_b^* dt. \quad (25)$$

At last,  $\alpha\beta$  reference currents are

$$i_{s\alpha}^* = i_{sd}^* \cos(\delta_b^*) - i_{sq}^* \sin(\delta_b^*) \quad (26)$$

$$i_{s\beta}^* = i_{sd}^* \sin(\delta_b^*) + i_{sq}^* \cos(\delta_b^*). \quad (27)$$

So, the method calculates the value of (20) for each available switching vector. The switching vector that minimizes (20) is selected and applied. Naturally, in healthy operation, the converter presents eight available switching vectors ( $[q_1 q_2 q_3] =$  from  $[000]$  to  $[111]$ ). The  $\alpha\beta$  voltage components  $v_{s\alpha}(k+2)$  and  $v_{s\beta}(k+2)$  that compose each switching vector are given by

$$\begin{bmatrix} v_{s\alpha}(k+2) \\ v_{s\beta}(k+2) \end{bmatrix} = \sqrt{\frac{2}{3}} \begin{bmatrix} 1 & -\frac{1}{2} & -\frac{1}{2} \\ 0 & \frac{\sqrt{3}}{2} & \frac{\sqrt{3}}{2} \end{bmatrix} \begin{bmatrix} v_{s1}(k+2) \\ v_{s2}(k+2) \\ v_{s3}(k+2) \end{bmatrix} \quad (28)$$

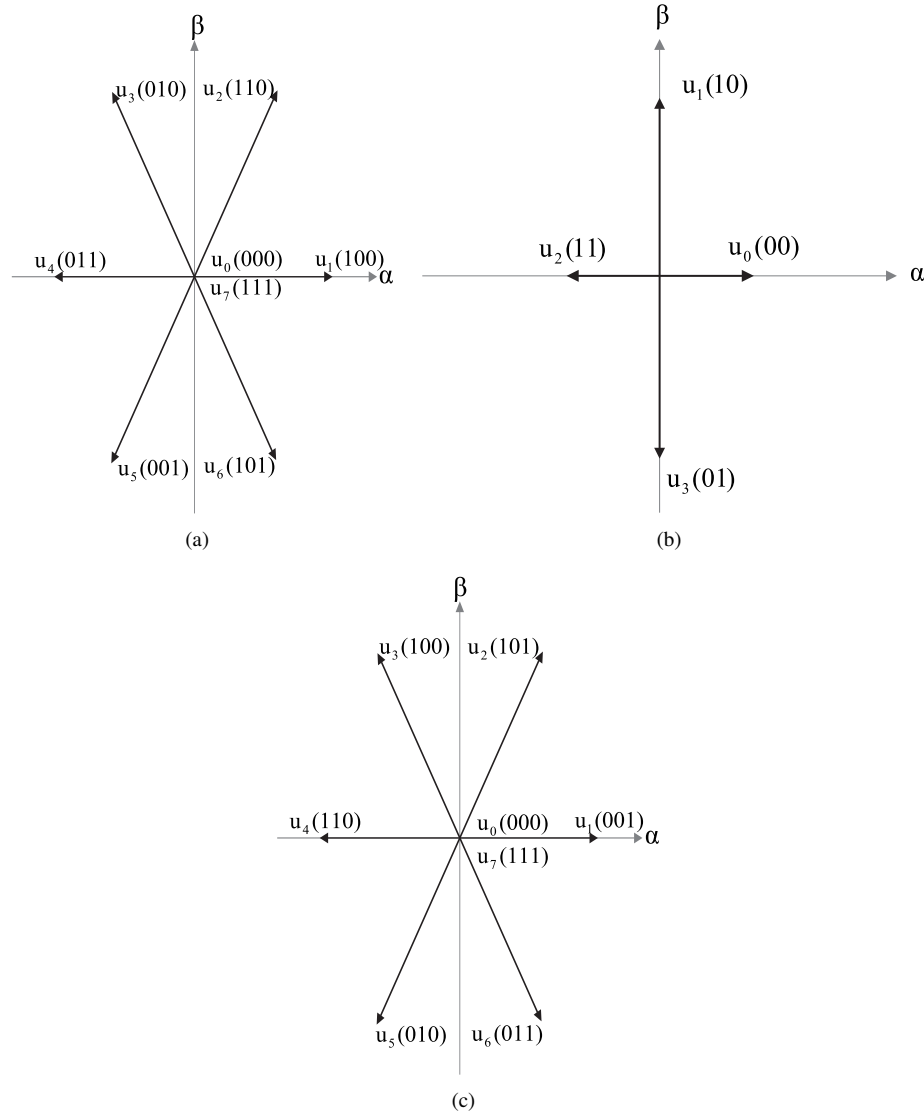


FIGURE 3. Switching vectors. (a) Healthy operation. (b) Faulty operation – configuration 1. (c) Faulty operation – configuration 2.

where  $v_{s1}(k+2)$ ,  $v_{s2}(k+2)$  and  $v_{s3}(k+2)$  are the predicted phase voltages. They are given as functions of the pole voltages. For healthy operation, the predicted pole voltages are:

$$v_{s10}(k+2) = (2q_1(k+2) - 1) \frac{v_C}{2} \quad (29)$$

$$v_{s20}(k+2) = (2q_2(k+2) - 1) \frac{v_C}{2} \quad (30)$$

$$v_{s30}(k+2) = (2q_3(k+2) - 1) \frac{v_C}{2}. \quad (31)$$

The neutral voltage is

$$v_{n0}(k+2) = \frac{v_{s10}(k+2) + v_{s20}(k+2) + v_{s30}(k+2)}{3}. \quad (32)$$

Thus, the predicted phase voltages are finally given by

$$v_{s1}(k+2) = v_{s10}(k+2) - v_{n0}(k+2) \quad (33)$$

$$v_{s2}(k+2) = v_{s20}(k+2) - v_{n0}(k+2) \quad (34)$$

$$v_{s3}(k+2) = v_{s30}(k+2) - v_{n0}(k+2). \quad (35)$$

In this way, it is possible to map all available switching vectors as shown in Figure 3.a. The length of all vectors for healthy operation is  $0.8165v_C$ .

#### A. Postfault Operation – Configuration 1

As aforementioned, for the postfault operation of configuration 1 the neutral point of the machine is connected to the dc-link mid-point as part of the compensation strategy, and the control algorithm must be reconfigured as well. In this case, the system presents four available switching vectors since one leg is disconnected from the machine. Considering that an open-circuit fault takes place in phase 1, the available switching states are  $[q_2q_3] =$  from  $[00]$  to  $[11]$ . Note that, since the neutral is connected to the dc-link mid-point, so  $v_{n0}(k+2) = 0$ . In this way phase voltages  $v_{s2}(k+2)$  and

$v_{s3}(k+2)$  in the healthy phases become

$$v_{s2}(k+2) = v_{s20}(k+2) \quad (36)$$

$$v_{s3}(k+2) = v_{s30}(k+2). \quad (37)$$

However, to obtain  $v_{s\alpha}(k+2)$  and  $v_{s\beta}(k+2)$  using (28), the faulty phase voltage  $[v_{s1}(k+2)]$  is still needed. It is known that even though phase 1 is disconnected from the converter, there is an induced voltage in its winding. By Faraday's law, this induced voltage is given by  $v_{s1}(t) = d\phi_{s1}(t)/dt$ , where  $\phi_{s1}(t)$  is the magnetic flux in phase 1. Using (1) and (2), the magnetic flux  $\phi_{s1}(k)$  calculated in the present calculation step is

$$\phi_{s1}(k) = \sqrt{2/3}(\phi_{s\alpha}(k) + \phi_{s\beta}(k)/\sqrt{2}) \quad (38)$$

and finally, the flux derivative is calculated numerically by

$$v_{s1}(k) = \frac{\phi_{s1}(k) - \phi_{s1}(k-1)}{T_s} \quad (39)$$

where  $\phi_{s\alpha}(k-1)$  is the magnetic flux value in the previous step.

Thus, in this case, considering that the sampling frequency is high and that the induced voltage in the faulty phase has a near-sinusoidal waveform,  $v_{s1}(k+2) = v_{s1}(k)$  and the values of  $v_{s\alpha}(k+2)$  and  $v_{s\beta}(k+2)$  are obtained, allowing the calculation of predicted currents  $i_{s\alpha}(k+2)$  and  $i_{s\beta}(k+2)$  (using (14) and (15)) for all four available switching vectors. The switching vector that minimizes the cost function is selected and applied.

Additionally, the calculated  $v_{s1}(k)$  can also be used in the stator flux observer of [20]. In this way, contrarily to what was made in [15] for a PMSM, the machine model, the transformation matrix (2), and the flux observer do not need to be readapted for postfault operation, meaning that the same equations used in healthy operation are still valid.

### B. Postfault Operation – Configuration 2

At last, for configuration 2, the machine's neutral is connected to the extra leg  $s_n$  through a triac. In this case, eight switching vectors ( $[q_2q_3q_n]$  = from [000] to [111]) are available. The neutral voltage is a pole voltage given by

$$v_{n0}(k+2) = (2q_n(k+2) - 1)\frac{v_C}{2}. \quad (40)$$

Once again, considering that the fault takes place in phase 1, the voltages in the healthy phases are

$$v_{s2}(k+2) = v_{s20}(k+2) - v_{n0}(k+2) \quad (41)$$

$$v_{s3}(k+2) = v_{s30}(k+2) - v_{n0}(k+2). \quad (42)$$

And again, faulty phase voltage  $v_{s1}(k+2)$  is obtained by calculation of the flux derivative as shown in (39) and  $v_{s\alpha}(k+2)$  and  $v_{s\beta}(k+2)$  are calculated using (28).

Similarly to configuration 1, the system equations do not need to be readapted for postfault operation.

### C. Rotor Speed Controller Design

As aforementioned, the rotor speed is controlled using a conventional PI controller. The calculation of its proportional and integral gains uses performance criteria such as accommodation time and damping ratio, as explained in [21], and are given by:

$$k_{p\omega} = \frac{8\tau_\omega - t_{ac}}{t_{ac}\beta_\omega} \quad (43)$$

$$k_{i\omega} = \frac{16\tau_\omega}{t_{ac}^2\epsilon^2\beta_\omega} \quad (44)$$

where  $\tau_\omega$  is the rotor mechanical time constant ( $\tau_\omega = J_m/F_m$ , where  $J_m$  is the moment of inertia and  $F_m$  is the friction coefficient),  $t_{ac}$  is the control accommodation time,  $\beta_\omega = 1/F_m$ , and  $\epsilon$  is the damping ratio.

### V. SIMULATION RESULTS

Digital simulations using programming language C were performed for PCC and FOC methods for the fault-tolerant configurations. The machine parameters are shown in Table 1, where  $L_{lr}$  is the rotor leakage inductance, making  $L_s = L_{ls} + L_m$  and  $L_r = L_{lr} + L_m$ . The dc-link voltage was 550 V. Reference rotor flux was  $\phi_r^* = 0.9$  Wb. The applied mechanical torque was -1.39 Nm. The negative value of torque means that the machine operated as a generator.

The inner control loop of the used FOC method was performed in the stationary reference frame and made by means of resonant-PI current controllers, as described in [22]. The current controllers' proportional and integral gains used in FOC were 56.51 and 39273, respectively.

In order to perform a fair comparison, the sampling frequency used for FOC simulations was adjusted in such a way that the obtained switching frequency becomes similar to the one observed when PCC is used. In this way, the sampling frequency of PCC was 10 kHz, which makes the switching frequency assume values near 2.5 kHz (approximately one-quarter of the sampling frequency). So, the sampling frequency used in FOC was made 2.5 kHz, making its switching frequency of 2.5 kHz (since the sampling frequency is equal to the switching frequency of the used PWM strategy in FOC).

For the rotor speed controller gains, the damping ratio was made  $\epsilon = 0.7$  in all cases. On the other hand, since the system dynamics of PCC is different from that of FOC since the current inner loop behaves differently for each method, the accommodation times for each method were set to provide a better dynamic response for each case. In this way, the accommodation time for PCC was  $t_{ac}=1.1$ s, making  $k_{p\omega}=0.093$  and  $k_{i\omega}=0.35$ . For FOC,  $t_{ac}=0.7$ s, making  $k_{p\omega}=0.15$  and  $k_{i\omega}=0.87$ .

As will be discussed in the following sections, in order to observe the systems' behavior when submitted to different operating conditions for both configurations, three scenarios of simulation were performed: Scenario 1) Transient-state results when the systems migrate from healthy operation to postfault operation with high rotation speed (250 rad/s, i.e.,



TABLE 1. Induction Machine Parameters

Parameter	Value
$r_s$	15.1 $\Omega$
$L_{ls}$	39.9 mH
$r_r$	6.22 $\Omega$
$L_{lr}$	39.9 mH
$L_m$	523.8 mH
$p$	1
$J_m$	0.013 $kg.m^2$
$F_m$	0.001
Rated power	500 W

approximately 2400 rpm); Scenario 2) Transient-state results when the systems migrate from healthy operation to postfault operation with low rotation speed (41.88 rad/s, i.e., approximately 400 rpm); Scenario 3) Steady-state results, showing the phase current THD and torque ripple as a function of the generated power for postfault operation. Scenarios 1, 2, and 3 bring a performance comparison between PCC and FOC.

### A. Migration from Healthy to Postfault Operation

#### 1) High Rotation speed – Scenario 1

Considering the first scenario for both PCC and FOC methods, the results for configuration 1 are shown in Figure 4.a and 4.b for PCC and FOC, respectively, and the results for configuration 2 are shown in Figure 4.c and 4.d for PCC and FOC, respectively. The systems operate in healthy condition until the time of 5s. At this moment, an open-circuit fault takes place in phase 1, making its current assume null value ( $i_{s1} = 0$ ), as shown in the left curves in Figure 4. From 5s to 5.1s, the system operated without compensation strategy, i.e., the triac was still blocked, and the control algorithm was the same as healthy operation. This causes high oscillation in current and torque. At 5.1s, the system reconfiguration is activated, meaning that the triac was triggered and post-fault control algorithm was employed.

As can be seen, the compensation strategy makes  $\alpha\beta$  currents present the same waveforms as those in healthy operation, leading to low torque oscillation, characterizing fault-tolerant operation. This means the fault compensation strategy performed successfully for PCC and FOC. In this way, the applicability of Predictive Current Control for fault-tolerant systems is attested. However, it can be noted that PCC provides a much smoother transition, with lower current peaks and lower speed and torque oscillations than FOC, confirming that PCC has a better transient response in this scenario.

#### 2) Low rotation speed – Scenario 2

On the other hand, the second scenario was performed for a rotor speed of 41.88 rad/s. The results for configuration 1 are shown in Figure 5.a and 5.b for PCC and FOC, respectively, and the results for configuration 2 are shown in Figure 5.c

and 5.d for PCC and FOC, respectively. An open-circuit fault takes place in phase 1 at 3.5s. From 3.5s to 3.6s, the system operates without compensation strategy. At 3.6s, the system is reconfigured, meaning the compensation strategy is activated.

In this scenario, for both configurations, PCC rapidly responded to the activation of the compensation strategy, making  $\alpha\beta$  currents assume virtually the same waveforms as before the fault, with low speed and torque oscillations. On the other hand, when FOC is used, the systems take a long time to reach post-fault steady state, since  $\alpha\beta$  currents and rotor speed take, respectively, almost 2s and 6s to assume their reference values, and high speed and torque oscillations are observed, even with the activation of the compensation strategy. In this way, PCC also has a better dynamic response than FOC in this scenario.

### B. Steady-State Analysis – Total Harmonic Distortion and Torque Ripple – Scenario 3

At last, the third simulation scenario provided the phase current THD and torque ripple for postfault operation when PCC and FOC are applied for both configurations. Actually, for the case of FOC, the steady-state values are more affected by the PWM strategy that is employed than by the control method itself. In this case, the used PWM strategy was the conventional Carrier Based-PWM (CB-PWM), as discussed in [23].

In this way, the THD value was calculated by

$$THD = \frac{\sqrt{I_{rms}^2 - I_1^2}}{I_1} 100\% \quad (45)$$

where  $I_{rms}$  is the rms current value and  $I_1$  is rms value of the current fundamental component.

To define the analyzed points of operation, nine different mechanical torque values were applied to make the generated real power vary from 0.1 pu to 0.9 pu during healthy operation. However, it must be highlighted that, although the same torque values were applied in postfault operation, the generated power values are lower than in healthy condition with the generated power varying from the minimum of 0.018 pu to a maximum of 0.43 pu. It happens because the zero-sequence current  $i_{so}$  is no longer null since the machine neutral is connected to either the dc-link mid-point (configuration 1) or an extra leg (configuration 2). Although necessary for the compensation strategy, this current component does not produce either torque or flux and contributes only to the machine losses. In this way, the generated power becomes lower for postfault operation for the same applied mechanical torque because of the higher losses in postfault operation when compared to those observed in healthy operation. In addition, it is possible to see that for the highest torque value (3.4 Nm), the generated power started to decrease due to the loss augmentation derived from  $i_{so}$ .

Figure 6.a shows the THD values for postfault operation when configuration 1 was used. PCC and CB-PWM performed very similarly, especially for the higher torque values.

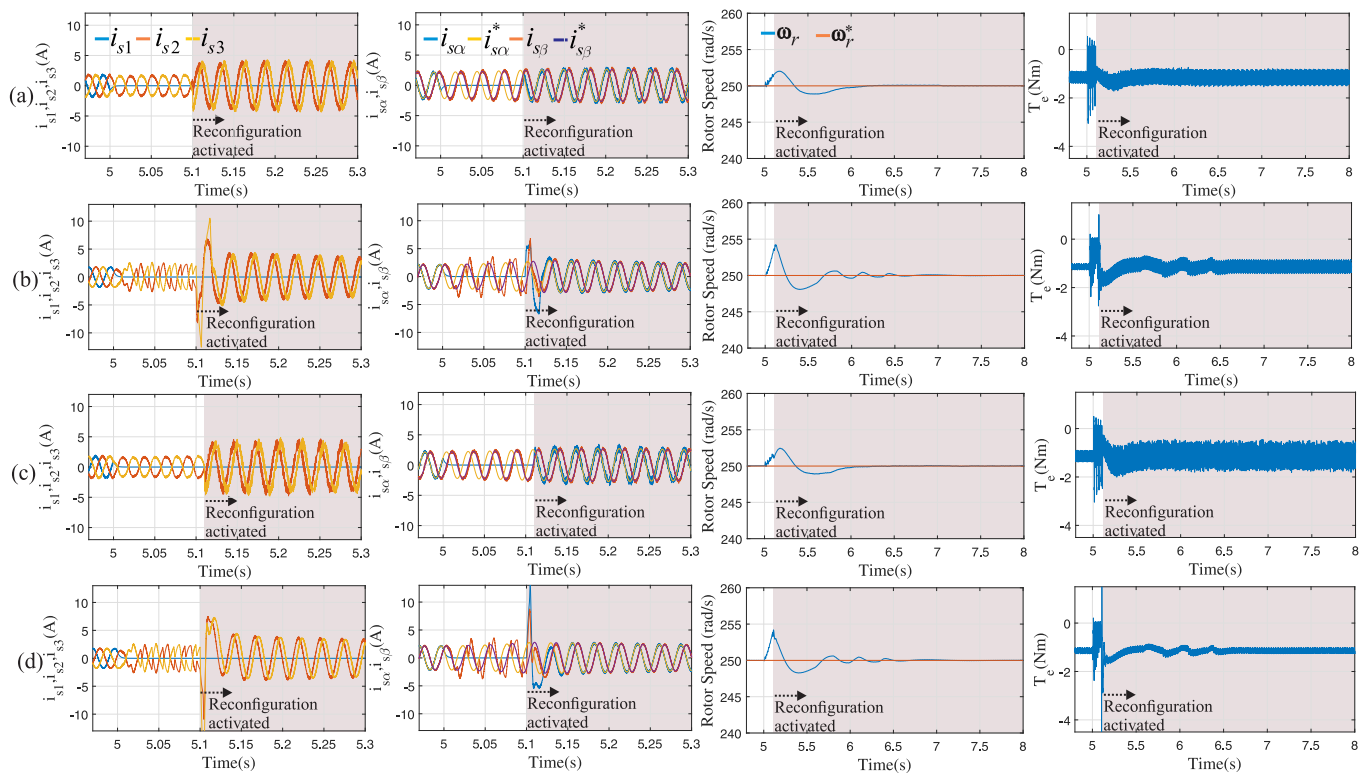


FIGURE 4. Migration from healthy to postfault operation – high rotation speed. (a) Conf. 1 – PCC. (b) Conf. 1 – FOC. (c) Conf. 2 – PCC. (d) Conf. 2 – FOC.

Overall, for configuration 1, PCC and CB-PWM have similar steady-state performance in terms of harmonic distortion.

For configuration 2, Figure 6.b shows the obtained THD values. In this case, CB-PWM provides lower distortion than PCC for all points of operation.

Concerning torque ripple value, it was calculated as

$$\Delta T_e = \frac{T_{e(p-p)}}{T_{e(avg)}} 100\% \quad (46)$$

where  $T_{e(p-p)}$  is the peak-to-peak torque variation and  $T_{e(avg)}$  is the torque average value.

Figures 7.a and 7.b show the postfault operation curves for configurations 1 and 2, respectively, for the same nine points of operation described before. CB-PWM presents lower torque ripple than PCC for configuration 2, but for configuration 1 the torque ripple values are very similar for both methods.

## VI. EXPERIMENTAL RESULTS

In order to prove the experimental feasibility of fault-tolerant operation using PCC method, configurations 1 and 2 were implemented experimentally. The experimental setup is shown in Figure 8. The power converter comprises 12 SEMIKRON SKM50GB12T4 IGBT modules. The voltage sensors are LEM LV20-P and the current sensors are LEM LTS15-NP. The three-phase induction generator has the same parameters of simulations, shown in Table 1. The mechanical torque was provided by a three-phase 0.56-kW induction motor, which is the prime mover. The control

algorithm was implemented in the Digital Signal Processor TMS320C28379D. The dc-link voltage was 550 V, the sampling frequency was 10 kHz. Reference rotor flux was  $\phi_r^* = 0.9$  Wb. The dc-link voltage was adjusted by a variac, a diode-based rectifier and a load resistor.

To attest the PCC fault-tolerant operation and its robustness, experiments were performed for four different scenarios: Scenario 1) Transient-state results when the systems migrate from healthy operation to postfault operation with high rotation speed (250 rad/s, i.e., approximately 2400 rpm); Scenario 2) Transient-state results when the systems migrate from healthy operation to postfault operation with low rotation speed (41.88 rad/s, i.e., approximately 400 rpm); Scenario 3) Robustness to parametric errors with high rotation speed during postfault operation; Scenario 4) Transient-state results to step variation in reference rotor speed during postfault operation.

### A. Migration from Healthy to Postfault Operation

#### 1) High rotation speed – Scenario 1

With a rotor speed of 250 rad/s (2400 rpm), Figures 9.a, 9.b, 9.c and 9.d show the phase currents, the  $\alpha\beta$  currents, the rotor speed, and the electromagnetic torque, respectively, for configuration 1. Similarly to what was made in simulations, the system initially operated in healthy operation. However, a single-phase open-circuit fault took place in phase 1, making current  $i_{s1}$  assume a null value. The system operated during some time in faulty operation before compensation.

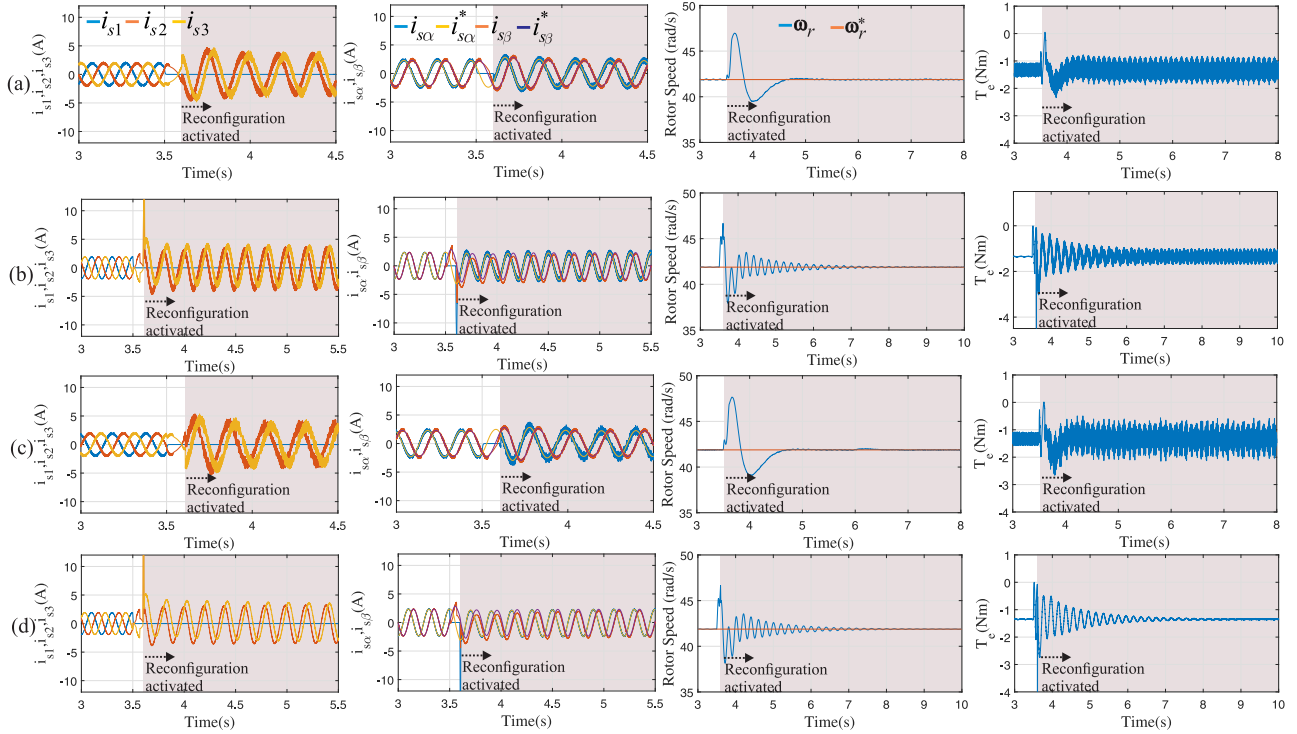


FIGURE 5. Migration from healthy to postfault operation – low rotation speed. (a) Conf. 1 – PCC. (b) Conf. 1 – FOC. (c) Conf. 2 – PCC. (d) Conf. 2 – FOC.

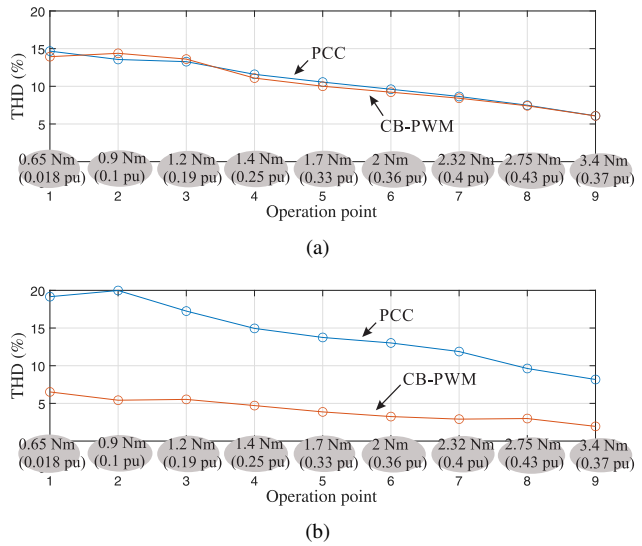


FIGURE 6. THD curves. (a) Faulty operation – configuration 1. (b) Faulty operation – configuration 2.

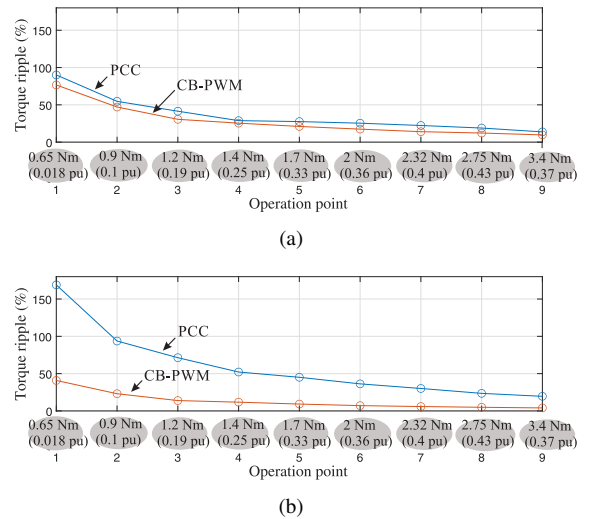


FIGURE 7. Torque ripple curves. (a) Faulty operation – configuration 1. (b) Faulty operation – configuration 2.

At last, the triac was fired, connecting the machine neutral to the dc-link mid-point, and the algorithm was reconfigured to perform the compensation strategy. The experimental results show that the  $\alpha\beta$  currents assume practically the same waveforms as before the fault, providing fault-tolerant operation. Also, the rotor speed is adjusted to the reference speed after a fast transient state due to the occurrence of the fault. Moreover, the electromagnetic torque continues to present a low ripple when the compensation strategy

is activated. In this way, the results shown in Figure 9 are in full accordance with simulation results presented in Figure 4.a. This shows that PCC method provides fault-tolerant operation and presents good steady and dynamic performances, presenting a smooth and fast transition from healthy to post-fault operation.

A similar procedure was made for configuration 2 and Figure 10 shows the same waveforms as configuration 1. Once again, the results are in full accordance with simulation results shown in Figure 4.c. In this way, the PCC method



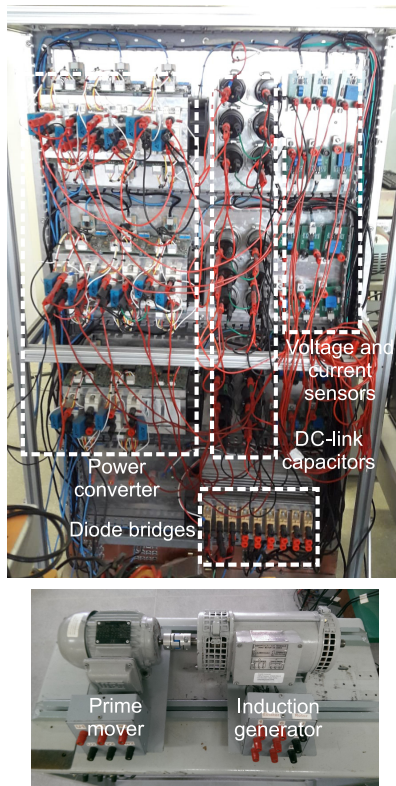


FIGURE 8. Experimental setup.

provided a smooth and fast transition from healthy to post-fault operation, and good steady-state performance.

## 2) Low rotation speed – Scenario 2

To prove the robustness of the PCC method when the system operates under single-phase open-circuit fault with low rotor speeds, experiments were performed with a rotor speed of 41.88 rad/s (400 rpm). For configurations 1 and 2, Figures 11 and 12, respectively, illustrated the phase currents,  $\alpha\beta$  currents, the rotor speed, and the electromagnetic torque for the transition from healthy to postfault operation when a fault takes place in phase 1. Similarly to the high rotor speed case, the  $\alpha\beta$  currents assume virtually the same waveforms as before the fault, characterizing fault-tolerant operation. Also, the rotor speed is adjusted to the reference value, and the torque presents a low torque ripple when the system reconfiguration is activated. For both configurations, the experimental results are in full accordance with the simulation results presented in Figures 5.a and 5.c.

### B. Robustness to Parametric Errors in Postfault Operation – Scenario 3

As explained in [7], accurately estimating the machine parameters may be complex, mainly because they may vary depending on the operation conditions, such as working temperature. In this way, it is essential to verify the robustness of the PCC method to possible parametric errors

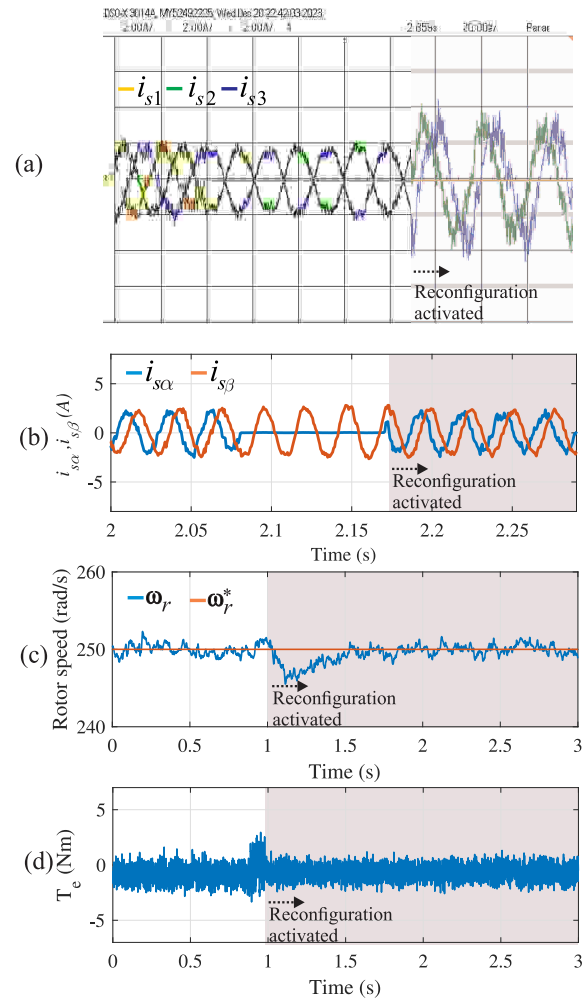


FIGURE 9. Experimental results – PCC – Conf. 1 – high rotation speed. (a) Phase currents. (b)  $\alpha\beta$  currents. (c) Rotor speed ( $\omega_r$ ). (d) Electromagnetic torque ( $T_e$ ).

since it depends strongly on the system model. The analysis performed in the present paper evaluated the impact of errors in estimating the stator resistance and the mutual inductance for postfault operation with high rotation speed (250 rad/s) for both configurations. The systems operate in postfault condition, meaning that the triac was already activated, as well as the algorithm reconfiguration.

Initially, for configuration 1, the stator resistance value was changed in the model used in the control algorithm as shown in Figure 13.a. The value of the  $r_s$  was 15.1  $\Omega$  until 0.5s, and it started to increase until it reached the value of 21.7  $\Omega$  at 3.5s, representing an increase of 43.17 %. As can be seen, the system presents good robustness to the evaluated parametric interval since the rotor speed and torque remain stable, as shown in Figures 13.b and 13.c, respectively.

The same  $r_s$  variation was performed for configuration 2. The obtained results are shown in Figure 14. Once again, the system presents good robustness to the evaluated parametric interval.

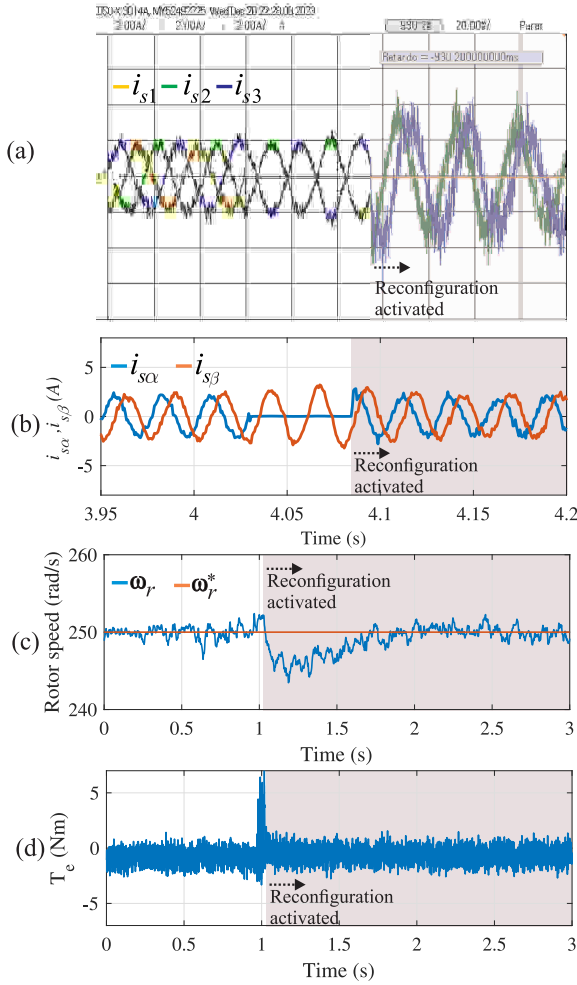


FIGURE 10. Experimental results – PCC – Conf. 2 – high rotation speed. (a) Phase currents. (b)  $\alpha\beta$  currents. (c) Rotor speed ( $\omega_r$ ). (d) Electromagnetic torque ( $T_e$ ).

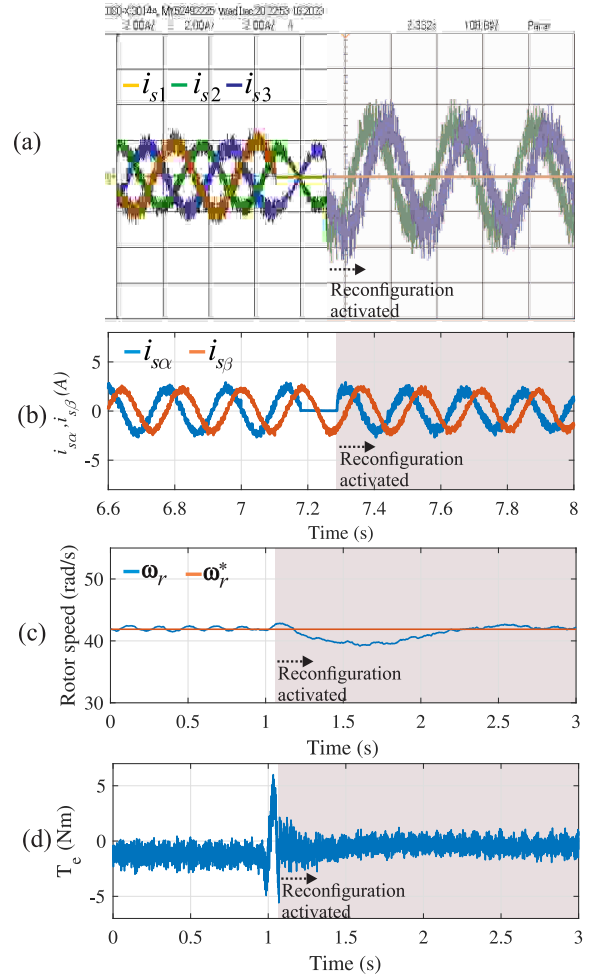


FIGURE 11. Experimental results – PCC – Conf. 1 – low rotation speed. (a) Phase currents. (b)  $\alpha\beta$  currents. (c) Rotor speed ( $\omega_r$ ). (d) Electromagnetic torque ( $T_e$ ).

Now, once again, for configuration 1, the mutual inductance  $L_m$  had its value changed in the model used in the control algorithm, as shown in Figure 15.a. The value of  $L_m$  was 523.8 mH until 0.5s, and it started to increase until it reached the value of 1 H at 3.5s, representing an increase of 90.91 %. As can be seen, configuration 1 presented good robustness to the evaluated parametric interval since the rotor speed and torque remain stable, as shown in Figures 15.b and 15.c, respectively.

The same  $L_m$  variation was performed for configuration 2. The results are shown in Figure 16. Once again, the system presents good robustness to the evaluated parametric interval.

### C. Transient-State Performance to Step Variation in Reference Rotor Speed – Scenario 4

For postfault operation, in this scenario, configurations 1 and 2 were submitted to a step of reference rotor speed during postfault operation. The step consisted in changing the reference rotor speed from 41.88 rad/s (400 rpm) to

125.66 rad/s (1200 rpm). The results are shown in Figures 17 and 18 for configurations 1 and 2, respectively. The reference electromagnetic torque  $T_e^*$  was limited 0 Nm as maximum value to avoid current peaks and to assure power generation at all times. Also, the anti-windup technique was employed in the rotor speed controller, in which the integrative part of the controller is deactivated during the controller saturation, making the speed overshoot lower.

Note that PCC method provided a good transient response when submitted to speed step, properly adjusting the rotor speed to the reference value, as illustrated in Figures 17.a and 18.a. Low torque ripple is observed during the transition between the two rotor speed reference values (see Figures 17.b and 18.b), and as the rotor accelerates, the  $\alpha\beta$  currents increase their frequency (as expected), but always keeping the 90°-shift between them, showing that PCC assures fault-tolerant operation in this operating condition as well.

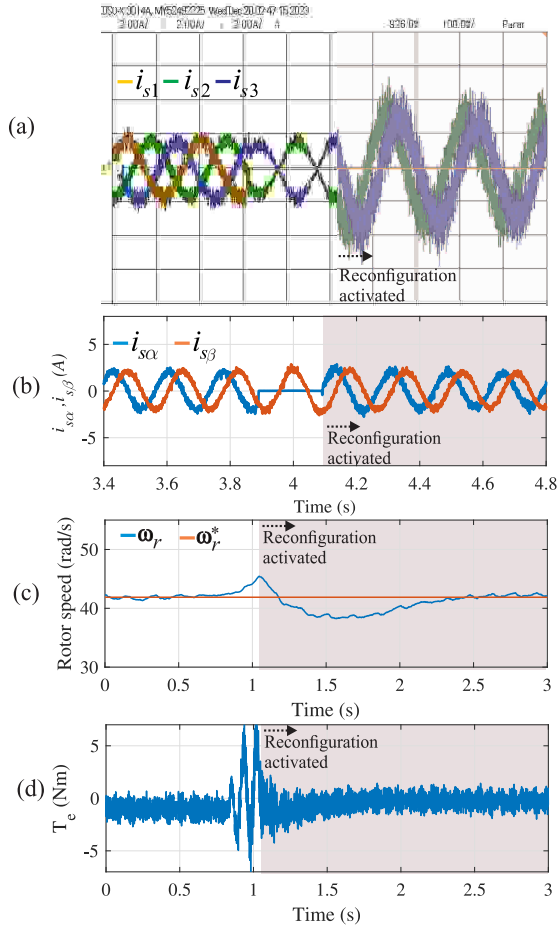


FIGURE 12. Experimental results – PCC – Conf. 2 – low rotation speed. (a) Phase currents. (b)  $\alpha\beta$  currents. (c) Rotor speed ( $\omega_r$ ). (d) Electromagnetic torque ( $T_e$ ).

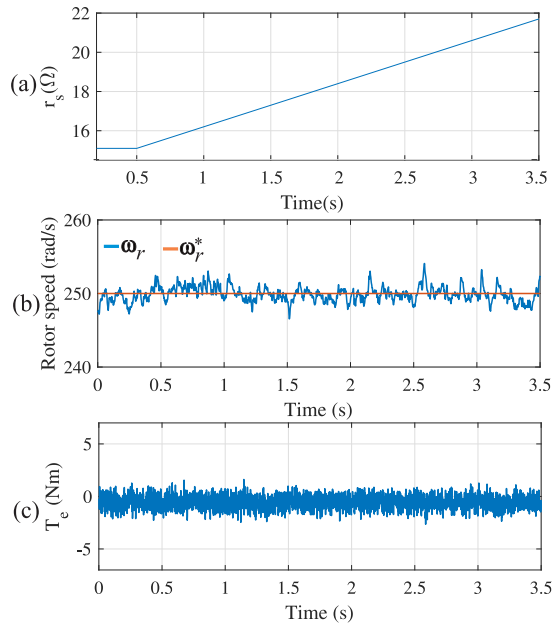


FIGURE 13. Variation of stator resistance – configuration 1. (a) Stator resistance ( $r_s$ ). (b) Rotor speed ( $\omega_r$ ). (c) Electromagnetic torque ( $T_e$ ).

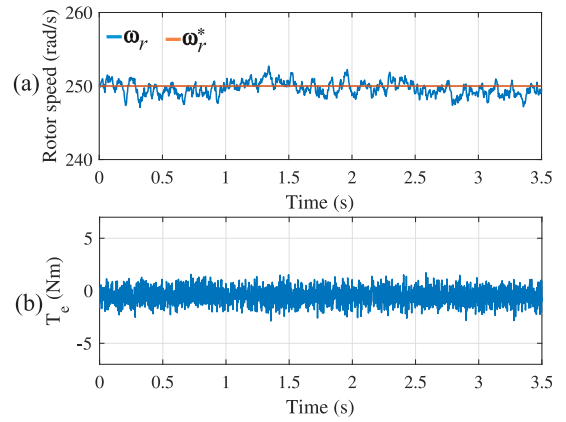


FIGURE 14. Variation of stator resistance – configuration 2. (a) Rotor speed ( $\omega_r$ ). (b) Electromagnetic torque ( $T_e$ ).

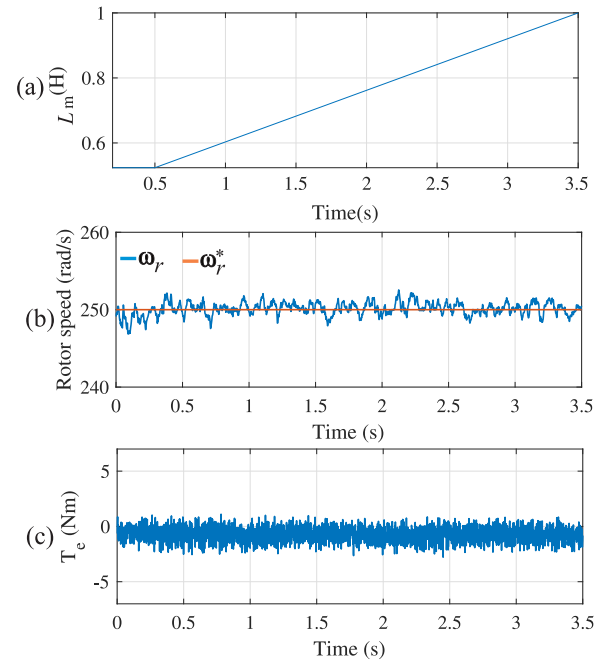


FIGURE 15. Variation of mutual inductance – configuration 1. (a) Mutual inductance ( $L_m$ ). (b) Rotor speed ( $\omega_r$ ). (c) Electromagnetic torque ( $T_e$ ).

## VII. CONCLUSION

This paper discussed the Predictive Current Control performance of two three-phase squirrel-cage fault-tolerant induction machine drive systems. The studies showed that this control method provided proper post-fault operation, since the  $\alpha\beta$  currents were adequately adjusted to present the same waveform as before the fault, leading to a low torque ripple. Also, a comparison between FOC and PCC was presented for both configurations for high and low rotation speeds, showing that PCC, besides showing a proper post-fault steady-state operation, also provides a much better transient response than FOC when the systems migrate from healthy operation to post-fault operation, with much lower current and torque oscillation.

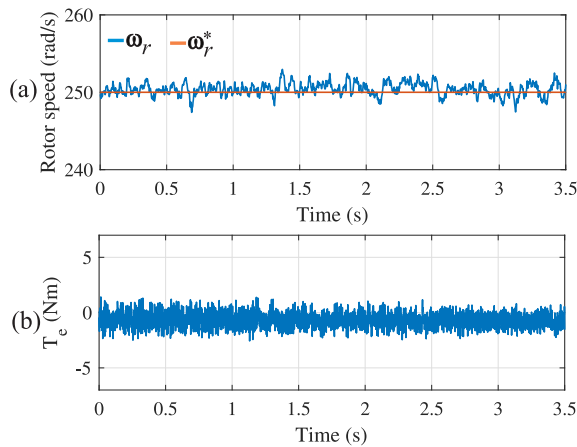


FIGURE 16. Variation of mutual inductance – configuration 2. (a) Rotor speed ( $\omega_r$ ). (b) Electromagnetic torque ( $T_e$ ).

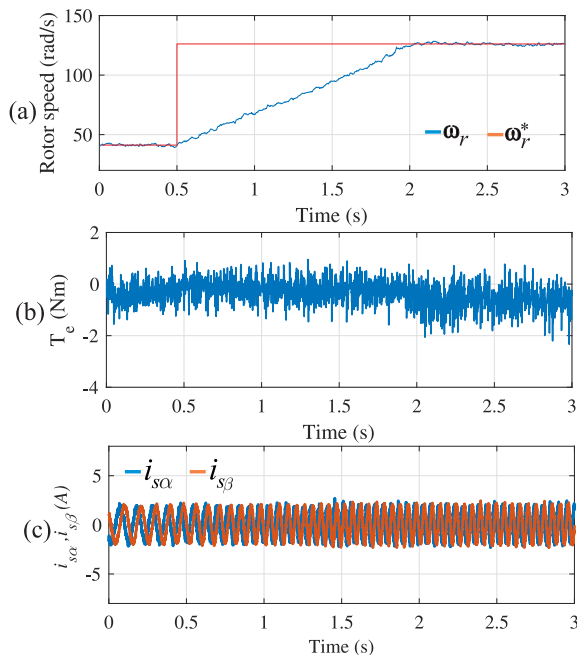


FIGURE 17. Step change in reference rotor speed – configuration 1. (a) Rotor speed ( $\omega_r$ ). (b) Electromagnetic torque ( $T_e$ ). (c)  $\alpha\beta$  currents.

To assess the postfault steady-state behaviour of the systems, phase current THD and torque ripple were calculated for nine different power generation operating points employing PCC and FOC+CB-PWM for the same switching frequency. Considering the configuration 1, PCC and CB-PWM presented a similar performance in terms of THD and torque ripple. On the other hand, for configuration 2, CB-PWM has lower distortion and torque ripple values than PCC for all considered operation points.

Also, in order to evaluate the PCC method postfault robustness to parametric errors, experiments were performed varying the values of stator resistance and mutual inductances used in the control algorithm. In the evaluated parametric intervals, the systems presented proper fault-tolerant

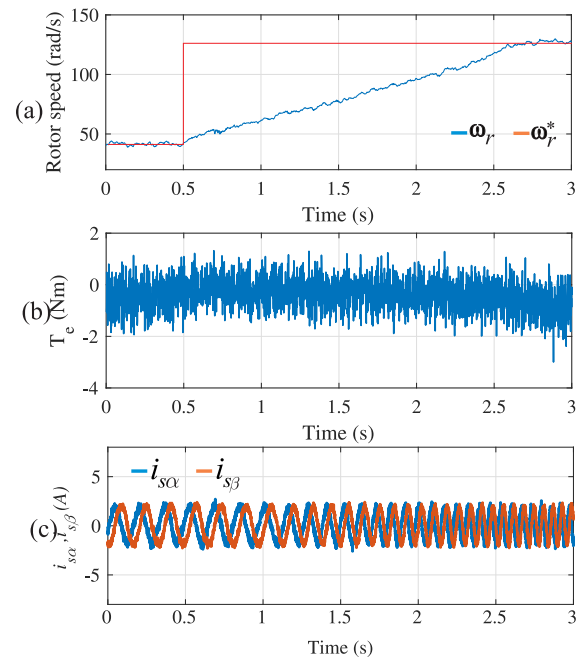


FIGURE 18. Step change in reference rotor speed – configuration 2. (a) Rotor speed ( $\omega_r$ ). (b) Electromagnetic torque ( $T_e$ ). (c)  $\alpha\beta$  currents.

operation, with low torque ripple and rotor speed adjusted to its reference value, then showing high robustness to parametric errors.

At last, the PCC method postfault dynamic response was evaluated submitting the systems to a step rotor speed change from 41.88 rad/s (400 rpm) to 125.66 rad/s (1200 rpm). The rotor speed was suitably adjusted to the new rotor speed reference value, showing that PCC assures proper system operation for this condition as well.

## ACKNOWLEDGMENTS

The authors would like to thank the National Council for Scientific and Technological Development – CNPq and IFPB – Campus Joao Pessoa for the financial support.

## AUTHOR'S CONTRIBUTIONS

Conceptualization, Formal Analysis, Investigation, Methodology: DE OLIVEIRA, L. M.; Data Curation, Software, Supervision, Validation, Writing – Original Draft, Writing – Review & Editing: MELO, V. F. M. B.; Validation: DA PAZ, G. F.; Validation: ROCHA, F. V.; Funding Acquisition, Writing – Review & Editing: FABRÍCIO, E. L. L. F.

## PLAGIARISM POLICY

This article was submitted to the similarity system provided by Crossref and powered by iThenticate—Similarity Check.

## REFERENCES

- [1] F. Blaschke, "A new method for the structural decoupling of A.C. induction machines", in *Conf. Rec. IFAC, Duesseldorf, Germany*, Oct. 1971.



- [2] M. Depenbrock, "Direct self-control (DSC) of inverter-fed induction machine", *IEEE Transactions on Power Electronics*, vol. 3, no. 4, pp. 420–429, Oct. 1988, doi:10.1109/63.17963.
- [3] I. Takahashi, T. Noguchi, "A New Quick-Response and High-Efficiency Control Strategy of an Induction Motor", *IEEE Transactions on Industry Applications*, vol. IA-22, no. 5, pp. 820–827, Sep. 1986, doi:10.1109/TIA.1986.4504799.
- [4] D. Casadei, F. Profumo, G. Serra, A. Tani, "FOC and DTC: two viable schemes for induction motors torque control", *IEEE Transactions on Power Electronics*, vol. 17, no. 5, pp. 779–787, Sep. 2002, doi:10.1109/TPEL.2002.802183.
- [5] J. Rodriguez, J. Pontt, C. A. Silva, P. Correa, P. Lezana, P. Cortes, U. Ammann, "Predictive Current Control of a Voltage Source Inverter", *IEEE Transactions on Industrial Electronics*, vol. 54, no. 1, pp. 495–503, Feb. 2007, doi:10.1109/TIE.2006.888802.
- [6] S. Kouro, P. Cortes, R. Vargas, U. Ammann, J. Rodriguez, "Model Predictive Control—A Simple and Powerful Method to Control Power Converters", *IEEE Transactions on Industrial Electronics*, vol. 56, no. 6, pp. 1826–1838, Jun. 2009, doi:10.1109/TIE.2008.2008349.
- [7] F. Wang, S. Li, X. Mei, W. Xie, J. Rodríguez, R. M. Kennel, "Model-Based Predictive Direct Control Strategies for Electrical Drives: An Experimental Evaluation of PTC and PCC Methods", *IEEE Transactions on Industrial Informatics*, vol. 11, no. 3, pp. 671–681, Apr. 2015, doi:10.1109/TII.2015.2423154.
- [8] F. Wang, H. Xie, Q. Chen, S. A. Davari, J. Rodríguez, R. Kennel, "Parallel Predictive Torque Control for Induction Machines Without Weighting Factors", *IEEE Transactions on Power Electronics*, vol. 35, no. 2, pp. 1779–1788, Jun. 2020, doi:10.1109/TPEL.2019.2922312.
- [9] M. Norambuena, J. Rodriguez, Z. Zhang, F. Wang, C. Garcia, R. Kennel, "A Very Simple Strategy for High-Quality Performance of AC Machines Using Model Predictive Control", *IEEE Transactions on Power Electronics*, vol. 34, no. 1, pp. 794–800, Mar. 2019, doi:10.1109/TPEL.2018.2812833.
- [10] A. Lunardi, A. Sguarezi Filho, "Controle Preditivo Baseado em Modelo para Sistema Eólico Empregando Gerador de Indução Gaiola de Esquilo", *Eletrônica de Potência*, vol. 23, no. 3, pp. 330–338, Sep. 2018, doi:10.18618/REP.2018.3.2788.
- [11] R. Figueiredo, A. Lunardi, A. S. Filho, A. Pelizari, "Controle Preditivo Robusto com Conjunto Finito de Estados para Máquinas de Indução", *Eletrônica de Potência*, vol. 27, no. 3, pp. 208–215, Ago. 2022, doi:10.18618/REP.2022.3.0027.
- [12] M. S. R. Saeed, W. Song, B. Yu, Z. Xie, X. Feng, "Low-Complexity Deadbeat Model Predictive Current Control for Open-Winding PMSM Drive With Zero-Sequence Current Suppression", *IEEE Transactions on Transportation Electrification*, vol. 7, no. 4, pp. 2671–2682, Apr. 2021, doi:10.1109/TTTE.2021.3071471.
- [13] C. M. Barros, W. Mota, P. Barros, L. Barros, "MPPT de Sistemas de Conversão de Energia Eólica Baseado em PMSG Usando Controle Preditivo", *Eletrônica de Potência*, vol. 20, no. 4, pp. 364–372, Nov. 2015, doi:10.18618/REP.2015.4.2553.
- [14] B. A. Welchko, T. A. Lipo, T. M. Jahns, S. E. Schulz, "Fault tolerant three-phase AC motor drive topologies: a comparison of features, cost, and limitations", *IEEE Transactions on Power Electronics*, vol. 19, no. 4, pp. 1108–1116, Jul. 2004, doi:10.1109/TPEL.2004.830074.
- [15] A. Kiselev, G. R. Catuogno, A. Kuznietsov, R. Leidhold, "Finite-Control-Set MPC for Open-Phase Fault-Tolerant Control of PM Synchronous Motor Drives", *IEEE Transactions on Industrial Electronics*, vol. 67, no. 6, pp. 4444–4452, Jul. 2020, doi:10.1109/TIE.2019.2931285.
- [16] Y. Guo, L. Wu, X. Huang, Y. Fang, J. Liu, "Adaptive Torque Ripple Suppression Methods of Three-Phase PMSM During Single-Phase Open-Circuit Fault-Tolerant Operation", *IEEE Transactions on Industry Applications*, vol. 56, no. 5, pp. 4955–4965, Jun. 2020, doi:10.1109/TIA.2020.3004305.
- [17] P. H. M. Martins, V. F. M. B. Melo, G. F. Paz, I. S. Freitas, "Direct-Torque-Control Fault-Tolerant Strategies for Three Induction Motor Drive Systems Operating Under Single-Phase Open-Circuit Fault", in *Brazilian Conference on Automatic (CBA 2020)*, 2020.
- [18] M. Tousizadeh, H. S. Che, J. Selvaraj, N. A. Rahim, B.-T. Ooi, "Performance Comparison of Fault-Tolerant Three-Phase Induction Motor Drives Considering Current and Voltage Limits", *IEEE Transactions on Industrial Electronics*, vol. 66, no. 4, pp. 2639–2648, Jul. 2019, doi:10.1109/TIE.2018.2850006.
- [19] L. M. de Oliveira, V. F. M. B. Melo, G. F. da Paz, F. V. Rocha, E. L. L. Fabrício, "Predictive Current Control Applied to Induction Machine Drive Systems Operating Under Single-Phase Open-Circuit Fault", in *Brazilian Power Electronics Conference (COBEP 2021)*, pp. 1–8, 2021, doi:10.1109/COBEP53665.2021.9684113.
- [20] X. Wu, W. Huang, X. Lin, W. Jiang, Y. Zhao, S. Zhu, "Direct Torque Control for Induction Motors Based on Minimum Voltage Vector Error", *IEEE Transactions on Industrial Electronics*, vol. 68, no. 5, pp. 3794–3804, Apr. 2021, doi:10.1109/TIE.2020.2987283.
- [21] K. Ogata, *Modern Control Engineering: Fifth Edition*, Pearson, Upper Saddle River, USA, 2010.
- [22] C. Jacobina, M. de Rossiter Correa, R. Pinheiro, E. da Silva, A. Lima, "Modeling and control of unbalanced three-phase systems containing PWM converters", *IEEE Transactions on Industry Applications*, vol. 37, no. 6, pp. 1807–1816, Nov.–Dec. 2001, doi:10.1109/28.968195.
- [23] E. R. C. da Silva, E. C. dos Santos, B. Jacobina, "Pulsewidth Modulation Strategies", *IEEE Industrial Electronics Magazine*, vol. 5, no. 2, pp. 37–45, Jun. 2011, doi:10.1109/MIE.2011.941120.

## BIOGRAPHIES

**Liane Marques de Oliveira** received her B.S. degree in Renewable Energies Engineering from the Federal University of Paraíba in 2022 and is currently working on her M.S. degree in the Postgraduate Program in Renewable Energies in the same institution. Her current research interests are optimization algorithms for battery energy management systems.

**Victor Felipe Moura Bezerra Melo** was born in Pesqueira, Brazil, in 1988. He received the B.S., M.S., and Ph.D. degrees in electrical engineering from the Federal University of Campina Grande, Campina Grande, Brazil, in 2012, 2013, and 2017, respectively. From October 2014 to June 2018, he was with the Federal Institute of Technology of Pernambuco, Afogados da Ingazeira, Brazil, where he was a Professor. Since June 2018, he has been with Renewable Energy Engineering Department, Federal University of Paraíba, João Pessoa, Brazil, where he is currently a Professor. His current research interests include multiphase drives, wind energy systems.

**Gilnelson Figueiredo da Paz** was born in João Pessoa, Paraíba, Brazil, in 1988. He received the B.S. degree in electrical engineering from the Federal Institute of Education, Science and Technology of Paraíba, João Pessoa, Brazil, in 2018 and Master's Degree from the Federal University of Paraíba, in 2020. He is currently a PHD Degree student at the Federal University of Campina Grande in the power electronics area. His interests include modeling and control of multiphase machines, machine drives, DC-AC power conversion, renewable energy sources, Converters AC-DC-AC, Unified Power Quality Conditioner and Active Filters.

**Filipe Vieira Rocha** received his B.S. degree in Electrical Engineering from the Federal University of Campina Grande, Brazil, in 2017, his M.S. degree from the Federal University of Paraíba, Brazil, in 2019, and his Ph.D degree from the Federal University of Campina Grande in 2023. His main research interests are power electronics, electric machine drives, and renewable energy.

**Edgard Luiz Lopes Fabricio** was born in João Pessoa, Paraíba, Brazil, in 1986. He received the B.S., M.S., and Ph.D. degrees in electrical engineering from the Federal University of Campina Grande, Brazil, in 2010, 2011, and 2015, respectively. Since 2012, he has been with the Academic Unity of Control and Industrial Processes, Federal Institute of Paraíba, João Pessoa, where he is currently a Professor of electrical engineering. His research interests include power electronics, energy systems, active power filter, and electrical drives.